

AperTO - Archivio Istituzionale Open Access dell'Università di Torino

**Intimate Binding Mechanism and Structure of Trigonal Nickel(I) Monocarbonyl Adducts in ZSM-5 Zeolite—Spectroscopic Continuous Wave EPR, HYSCORE, and IR Studies Refined with DFT Quantification of Disentangled Electron and Spin Density Redistributions along  $\sigma$  and  $\pi$  Channels**

**This is the author's manuscript**

*Original Citation:*

*Availability:*

This version is available <http://hdl.handle.net/2318/138384> since 2016-01-07T18:21:37Z

*Published version:*

DOI:10.1021/ja405874t

*Terms of use:*

Open Access

Anyone can freely access the full text of works made available as "Open Access". Works made available under a Creative Commons license can be used according to the terms and conditions of said license. Use of all other works requires consent of the right holder (author or publisher) if not exempted from copyright protection by the applicable law.

(Article begins on next page)



UNIVERSITÀ DEGLI STUDI DI TORINO

This is an author version of the contribution published on:

Piotr Pietrzyk, Tomasz Mazur, Katarzyna Podolska-Serafin, Mario Chiesa, Zbigniew Sojka

Intimate Binding Mechanism and Structure of Trigonal Nickel(I) Monocarbonyl Adducts in ZSM-5 Zeolite? Spectroscopic Continuous Wave EPR, HYSCORE, and IR Studies Refined with DFT Quantification of Disentangled Electron and Spin Density Redistributions along ? and ? Channels

JOURNAL OF THE AMERICAN CHEMICAL SOCIETY (2013) 135

DOI: 10.1021/ja405874t

The definitive version is available at:

<http://pubs.acs.org/doi/abs/10.1021/ja405874t>

Intimate Binding Mechanism and Structure of  
Trigonal Nickel(I) Monocarbonyl Adducts in ZSM-5  
Zeolite – Spectroscopic CW-EPR, HYSCORE and  
IR Studies Refined with DFT Quantification of  
Disentangled Electron and Spin Density  
Redistributions along  $\sigma$  and  $\pi$  Channels

*Katarzyna Podolska,<sup>1</sup> Tomasz Mazur,<sup>1</sup> Piotr Pietrzyk,<sup>1,\*</sup> Mario Chiesa,<sup>2</sup> and Zbigniew Sojka<sup>1</sup>*

<sup>1</sup> Faculty of Chemistry, Jagiellonian University, ul. R. Ingardena 3, 30-060 Krakow, Poland

<sup>2</sup> Dipartimento di Chimica, Università di Torino and NIS Centre of Excellence, via P. Giuria 7,  
10125, Torino, Italy

## ABSTRACT

Interaction of a tetraordinated nickel(I) site generated inside the NiZSM-5 zeolite channels with carbon monoxide ( $^{12,13}\text{CO}$ ) under low pressures ( $p_{\text{CO}} < 1$  Torr) led to the formation of a top-on  $\eta^1$  monocarbonyl adduct with a unique trigonal nickel core supported by two oxygen donor ligands. A mechanism of formation of the  $\{\text{Ni}_{3c}^{\text{I}}\text{-CO}\}$ ZSM-5 species was accounted for by means of the quantitative molecular orbital correlation diagram of CO ligation. Detailed electronic and magnetic structure of this adduct was obtained from comprehensive relativistic DFT calculations based on reproduction of its spectroscopic CW-EPR, HYSCORE, and IR fingerprints. Molecular analysis of the stretching frequency,  $\nu_{\text{CO}} = 2109 \text{ cm}^{-1}$ , as well as  $g$ ,  $A(^{13}\text{C})$ , and  $Q(^{27}\text{Al})$  tensors ( $g_{xx} = 2.018$ ,  $g_{yy} = 2.380$ ,  $g_{zz} = 2.436$ ,  $A_{xx} = +1.0 \pm 0.3 \text{ MHz}$ ,  $A_{yy} = -3.6 \pm 0.9 \text{ MHz}$ ,  $A_{zz} = -1.6 \pm 0.3 \text{ MHz}$ ,  $e^2Qq/h = -13 \pm 1 \text{ MHz}$ , and  $\eta = 0.9 \pm 0.2$ ) supported by quantum chemical modeling revealed that binding of CO is accompanied by a dramatic change of the coordination state of the parent nickel(I) center, caused by breaking of two bonds with the zeolite framework (alterdesmic ligation). The vacant coordination sites allow for straightforward top-on attachment of the carbon monoxide molecule, resulting in a **T**-conformation of the adduct, featured by a concerted rearrangement of the spin and charge between 3d orbitals (strong internal relaxation of the metal core). The binding of CO results from the  $\pi$  overlap between low-lying  $\pi(2p)$  CO states with the  $3d_{xz}$  and  $3d_{yz}$  orbitals of nickel, enhanced by small contribution due to the  $\sigma$  overlap between the  $\sigma(2p+2s)$  orbital and a protruding lobe of the in-plane  $3d_{xz}$  orbital. Two types of orbital channels (associated with  $\sigma$  and  $\pi$  overlap) of electron and spin density flows within the  $\{\text{Ni}^{\text{I}}\text{-CO}\}$  unit were identified using the natural orbitals for chemical valence

(NOCV) analysis, and their individual energetic relevance was quantified. A bathochromic shift of the stretching vibration of the carbonyl moiety was accounted for by resolving the separate contributions due to  $\sigma$  donation and  $\pi$  back-donation effects in a quantitative way, whereas the carbon-13 hyperfine coupling was rationalized by incongruent  $\alpha$  and  $\beta$  spin flow via the  $\sigma$  channel. Relativistic ZORA-SOMF/B3LYP calculations were used for prediction of the electronic  $g$  and hyperfine tensors. The characteristic magnetic structure of the adduct with  $g_{zz}(g_{\max}) > g_{yy}(g_{\text{mid}}) \gg g_{xx}(g_{\min})$  was analyzed in detail by means of a magnetic orbitals diagram based on the Pauli Hamiltonian calculations. As a result the very nature of the carbon-metal bond in Ni(I)-CO, and the molecular backbone of the corresponding spectroscopic parameters were revealed with an unprecedented accuracy for the first time.

## 1. Introduction

Among catalyzed reactions, those involving carbon monoxide have recently been the subject of intensive investigations at both fundamental and applied levels.<sup>1,2,3,4,5,6</sup> They concern both coordination and organometallic chemistry<sup>3,4,6</sup> as well as heterogeneous catalysis: selective catalytic reduction (SCR),<sup>5</sup> oxidation of CO,<sup>7,8,9</sup> methanol synthesis and CO hydrogenation,<sup>10</sup> or preferential oxidation of carbon monoxide in the presence of hydrogen (PROX reaction).<sup>11,12</sup> Owing to high sensitivity of its stretching vibration to charge redistribution upon bonding, carbon monoxide is also widely used as an excellent probe molecule for characterization of the valence and coordination states of transition metals in zeolites,<sup>13</sup> supported oxides,<sup>14</sup> and also for probing local electrostatic field strength via vibrational Stark effect.<sup>15</sup>

Nickel-exchanged zeolites attract increasing attention owing to their activity in deNO<sub>x</sub>,<sup>5,16</sup> olefin dimerization<sup>17</sup> or carbon dioxide reforming of methane.<sup>18</sup> Nickel(I) carbonyls, in particular, are the key species involved in many enzymatic and catalytic processes.<sup>19,20</sup> For instance, homogeneous Ni<sup>I</sup>-carbonyls of biologically relevant complexes can mimic the activity of acetylcoenzyme A (acetyl-CoA) synthases<sup>21</sup> or dihydrogen oxidation by hydrogenases.<sup>22</sup> Elucidation of reversible or irreversible character of carbon monoxide binding for these processes is of the key concern for such systems.<sup>23</sup> Low coordination number of the metal center and space confinement effects imposed by the framework on the intrazeolite nickel-carbonyl complexes, in turn, allow for studying their unique stereochemistry that is not easily obtainable in homogeneous conditions.

Vibrational description of the carbonyl coordination chemistry of dispersed nickel cations has been summarized elsewhere.<sup>14</sup> The carbonyl adducts with Ni<sup>2+</sup> give rise to IR bands located at 2220 - 2180 cm<sup>-1</sup> region. They are destroyed at ambient temperature, probably due to the lack of stabilizing  $\pi$  back-donation, in contrast to much more stable CO adducts of monovalent nickel,

observable in the 2160 - 2050  $\text{cm}^{-1}$  region. It is usually argued that their enhanced stability is caused by the interplay between the  $\sigma$  and  $\pi$  electronic interactions, although those processes have not been quantified separately as yet.

Depending on the nature of the coligands, the carbonyl complexes of tricoordinate  $\text{Ni}^{\text{I}}$  can adopt a **Y**-shaped or a **T**-shaped geometry.<sup>6,21,24</sup> It has also been found that the **Y** or **T** conformations involve a significant difference in the electronic structure and reactivity of the three-coordinate complexes in ligand substitution and transmetalation reactions, constituting an essential factor in the structural and kinetic studies.<sup>25,26</sup> Therefore, taking into account a far going analogy between the intrazeolite and enzymatic congeners,<sup>27</sup> to comprehend the fundamental chemistry of the  $\{\text{Ni}^{\text{I}}\text{-CO}\}$  unit for sensible control of its reactivity, a detailed molecular level description of its geometry, electronic and magnetic properties is of a great cognitive value.

Among many various methods applied to investigate the systems hosting the  $\{\text{Ni}^{\text{I}}\text{-CO}\}$  adducts, electron paramagnetic resonance (EPR) related spectroscopies are obviously prime techniques of choice due to the paramagnetic nature of those species.<sup>21</sup> However, an in-depth interpretation of the EPR spectral parameters in terms of the molecular structure of the corresponding complexes is not a trivial task, taking into account an intricate nature of the magnetic interactions within the metal-ligand unit and constraints imposed by low symmetry. Yet, owing relativistic DFT methods, calculations of EPR parameters are becoming nowadays accessible even for larger systems containing transition-metal ions.<sup>28</sup> The recent progress in this field has been reviewed by us elsewhere.<sup>29</sup> Calculations of the  $g$  tensor for nickel(I) complexes have focused so far mostly on biomimetic systems,<sup>6,30</sup> homogeneous complexes,<sup>31</sup> and paramagnetic Ni adducts with NO ligands.<sup>32</sup> It has been shown that conceptually useful results can also be obtained by analyzing simpler models such as  $\text{Ni}^{\text{I}}(\text{CO})_n\text{L}_m$  adducts ( $n = 1 \div 4$ ,  $L = \text{H}_2\text{O}$ ,  $\text{OH}^-$ ) epitomizing broad range of the conceivable chemical environments.<sup>33</sup> Having

established the principal relations between the electronic nature of the  $g$  and  $A$  tensors and the stereochemistry of the well defined nickel-carbonyl model systems, they can be used as a useful reference for analysis of structurally more demanding real adducts.<sup>34</sup>

This paper is devoted to detailed description of an electronic and magnetic structure of the monocarbonyl complexes with monovalent nickel produced by adsorption of CO at low pressures ( $p_{\text{CO}} < 1$  Torr) on dehydrated, reduced Ni<sup>I</sup>ZSM-5 zeolite. The occurrence, identification, and spectroscopic properties of di-, tri- and tetracarbonyls, produced at higher CO pressures, will be discussed in a forthcoming paper. Herein, we investigated more closely the molecular nature of the  $g$  and <sup>13</sup>C hyperfine tensors of the {Ni<sup>I</sup>-CO} adducts in terms of the local symmetry and the coordination state of nickel, to provide a clear-cut evidence for their definite assignment. Frontier molecular orbital picture of CO ligation, quantification of the  $\sigma$  and  $\pi$  channels of electron density redistribution upon bonding, and detailed insight into the magnetic molecular orbitals that contribute to the experimentally observed  $g$  tensor anisotropy were also discussed.

## 2. Materials and Methods

**2.1 Materials.** Ni-exchanged ZSM-5 metallozeolite was obtained by a standard ion exchange method using Ni(NO<sub>3</sub>)<sub>2</sub> aqueous solution (0.1 M) and a parent ammonium form of the ZSM-5 zeolite (Zeolyst, Inc.) with the Si/Al ratio equal to 15 and 40. Final pH of the solution varied from 2 to 5. Chemical analysis by means of ICP-MS method revealed the Ni/Al exchange degrees of 54 and 40%, respectively. After drying in air, prior to the spectroscopic measurements, the samples were activated in vacuum of 10<sup>-5</sup> mbar at 773 K for 2 h (with the heating rate of 6 K/min), reduced with CO (Aldrich, 99.95%) at 673 K for 30 minutes and finally evacuated at 553



K. The monocarbonyl complexes were generated by exposure of the reduced samples to CO at low pressures (below 1 Torr).

**2.2 Spectroscopic methods.** FTIR spectra were recorded on a Bruker Tensor 27 spectrometer equipped with MCT detector (at a spectral resolution of  $2\text{ cm}^{-1}$ ). The samples in a form of self-supporting pellets were placed in an IR cell connected to a vacuum line where *in situ* thermal activation (773 K) followed by reduction in CO and subsequent evacuation were carried out. Adsorption of carbon monoxide was carried out at ambient temperature. All spectra were normalized to standard pellet mass (10 mg, density  $3.2\text{ mg/cm}^2$ ).

Continuous wave electron paramagnetic resonance (CW-EPR) spectra were recorded at 77 K with a Bruker ELEXSYS-E580 X-band spectrometer using a rectangular  $TE_{102}$  cavity with the 100 kHz field modulation. The microwave power of 1 – 10 mW and the modulation amplitude of 0.1 – 0.5 mT were applied. Computer simulations of the spectra were performed with the EPRsim32 program,<sup>35</sup> which calculates exact solutions for the spin-Hamiltonian by full matrix diagonalization. A hybrid search procedure combining genetic algorithm and Powell refinement was applied for optimization of the simulated spectra.

Pulse EPR experiment were performed on a Bruker ELEXSYS-E580 (microwave frequency of 9.76 GHz) equipped with a liquid-helium cryostat from Oxford Instruments. All measurements were performed at 5 K. Electron spin echo (ESE) detected EPR spectra were obtained with the two pulse sequence:  $\pi/2-\tau-\pi-\tau$ -echo with the microwave pulse lengths  $t_{\pi/2} = 16\text{ ns}$  and  $t_{\pi} = 32\text{ ns}$  and delay time  $\tau = 200\text{ ns}$ . Hyperfine sublevel correlation (HYSCORE)<sup>36</sup> experiments were carried out with a four pulse sequence:  $\pi/2-\tau-\pi/2-t_1-\pi-t_2-\pi/2-\tau$ -echo with the microwave pulse lengths  $t_{\pi/2} = 16\text{ ns}$  and  $t_{\pi} = 16$ . The time intervals  $t_1$  and  $t_2$  were varied with an increment of 16

ns starting from 96 ns up to 3296 ns. In order to avoid blind-spot effects various  $\tau$  values were chosen, and the obtained spectra were added up after Fourier transform. An eight-step phase cycling was selected in order to eliminate unwanted echoes. The obtained HYSORE spectra were baseline corrected, apodized with Hamming window, and zero filled. After a two-dimensional Fourier transformation, the absolute value spectra were calculated, and next simulated with the EasySpin software.<sup>37</sup>

### 2.3 DFT Modeling

Zeolite sites, acting as rigid multi-dentate mineral ligands for hosting the nickel(I) centers and nickel(I)-carbonyl adducts, were modeled using geometrically embedded clusters of various number of T-atoms (T = Si or Al). The clusters were cut off from a model of the MFI lattice (using Materials Studio, Accelrys), and the resulting dangling bonds were saturated with the hydrogen atoms. Those atoms were placed along the broken O-Si bonds at the equilibrium distance, and during the geometry optimization they were kept frozen in order to mimic the rigidity of the outer part of the ZSM-5 zeolitic framework. A cluster of the  $[\text{Si}_6\text{AlO}_8(\text{OH})_{12}]^-$  stoichiometry, referred to as **M7**, was used as a binding site for nickel ions, based on previous experimental results,<sup>38</sup> and widely used in previous DFT cluster modeling studies.<sup>39,40,41</sup>

Partial geometry optimization was carried out for the  $\text{Ni}^{\text{I}}[\text{Si}_6\text{AlO}_8(\text{OH})_{12}]$  and  $[\text{CO-Ni}^{\text{I}}][\text{Si}_6\text{AlO}_8(\text{OH})_{12}]$  models by means of the Gaussian 09<sup>42</sup> software at the spin-unrestricted level. The B3LYP<sup>43</sup> exchange-correlation potential and all-electron basis set with additional polarization functions, denoted as 6-311G(d,p),<sup>44</sup> were used. The structure of the cluster models were optimized with analytic gradients and Berny algorithm using GEDIIS method,<sup>45</sup> within the SCF electron density convergence criterion of  $10^{-6}$  a.u., a maximum force criterion of  $4.5 \cdot 10^{-4}$

a.u./Å, and a maximum displacement criterion of  $1.8 \cdot 10^{-3}$  Å. Vibrational analysis was carried out with the harmonic approximation from the second derivatives computed numerically (two steps with 0.001 Å).

Electron density redistribution upon CO bonding (quantification of  $\sigma$  and  $\pi$  donation effects) and population analysis was performed based on the natural orbitals for chemical valence combined with the Ziegler-Rauk extended transition state energy decomposition scheme (ETS-NOCV)<sup>46,47</sup> as implemented in ADF program suite (version 2009.01).<sup>48,49</sup> The ETS-NOCV analysis allows for separation and quantification of the electron charge transfer channels between the on purpose delineated interacting fragments, for example  $[\text{CO}]_{\text{frag}}$  and  $[\text{Ni}^{\text{II}}\text{M7}]_{\text{frag}}$ . In such a case the pairs of the natural orbitals for chemical valence ( $\Psi_{-k}, \Psi_k$ ) allows to factorize differential charge density,  $\Delta\rho$ , into the particular NOCV contributions ( $\Delta\rho_k$ )<sup>46</sup>

$$\Delta\rho(r) = \sum_{k=1}^{M/2} v_k [-\psi_{-k}^2(r) + \psi_k^2(r)] \quad (1)$$

where  $v_k$  and  $M$  stand for the NOCV eigenvalues and the number of basis functions, respectively. For the open-shell systems the summation of the  $\alpha$  and  $\beta$  electron densities should be carried out separately over the spin-orbitals of virtually the same symmetry, but not necessarily possessing the same  $v_k$  values as shown previously by us for the  $\{\text{Ni}^{\text{II}}-\text{O}_2^-\}$ ZSM-5 system.<sup>27</sup>

The  $g$  tensor values were calculated using the ORCA software.<sup>50</sup> The scalar relativistic ZORA corrections were applied for electron structure calculations, whereas the mean-field approximation (SOMF),<sup>51</sup> including both the spin-own-orbit and spin-other-orbit interactions in the exchange term, was used in accounting for the spin-orbit coupling (SOC) effects. In addition, one-component approach due to Schreckenbach and Ziegler<sup>52</sup> was applied for construction of the molecular magnetic field-induced coupling diagrams based on the Pauli Hamiltonian. The hyperfine coupling  $A$  tensor and the quadrupole parameters were calculated according to the

spin-density based formulation that in the case of the hyperfine interaction includes additionally the SOC contribution as a second-order property.<sup>53</sup> For the spectroscopic calculations B3LYP hybrid functional with the all-electron triple- $\zeta$  basis sets was used for all atoms except of nickel, where a more accurate CP(PPP)<sup>54</sup> basis set was employed.

### 3. Results and Discussion

#### 3.1 Structure of the nickel(I) sites

The monovalent nickel(I) sites in ZSM-5 channels were produced by reduction of parent nickel-oxo species with CO at 673 K ( $\text{Ni(II)-O-Ni(II)} + \text{CO} \rightarrow 2\text{Ni(I)} + \text{CO}_2$ ) followed by prolonged evacuation of the reduced samples at 553 K. The diagnostic well resolved nearly axial EPR spectrum of Ni(I) with  $g_{zz} > g_{xx,yy}$  is shown in Figure 1a. As discussed in our previous paper in more detail,<sup>27</sup> it consists of a dominant signal due to the isolated nickel(I) center with  $g_{xx} = g_{yy} = 2.098$ ,  $g_{zz} = 2.478$ , determined by computer simulation. An expected anisotropy in the  $x$ - $y$  plane is, however, barely manifested in the experimental X-band spectrum due to the linewidths broadening. Such rhombic distortion of the  $\mathbf{g}$  tensor is consistent with the rectangular deformation of the four-fold arrangement of the planar donor  $\text{O}_{(\text{Al,Si})}$  ligands ( $\text{C}_{2v}$  symmetry), caused by the presence of the Al atom in the 12-membered macrocyclic ring of the zeolite framework. The corresponding Ni- $\text{O}_{(\text{Si,Si})}$  bond lengths are equal to 2.282 and 2.197 Å, whereas the Ni- $\text{O}_{(\text{Al,Si})}$  bond lengths are equal to 2.102 and 2.116 Å. The composition of the SOMO =  $0.83|3d_{x^2-y^2}\rangle + 0.12|3d_{yz}\rangle + 0.03|3d_z^2\rangle + 0.01|3d_{xz}\rangle$  accounts well for the dominant axial component of the  $\mathbf{g}$  tensor, whereas the weak rhombic component is associated with the appreciable admixture of the  $|yz\rangle$  state. The calculated (ZORA-SOMF/B3LYP)  $\mathbf{g}$  tensor values

( $g_{xx} = 2.117$ ,  $g_{yy} = 2.153$  and  $g_{zz} = 2.324$ ) remain in a good agreement with their experimental counterparts.<sup>27</sup>

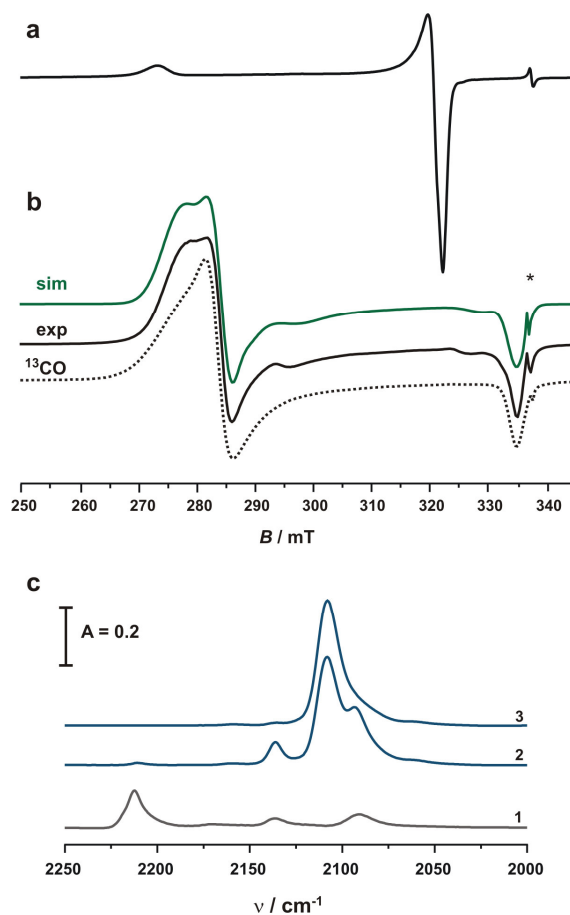


**Figure 1.** X-band CW EPR spectra (77 K) of (a) reduced Ni<sup>I</sup>ZSM-5 zeolite after prolonged evacuation, (b) after adsorption of <sup>12</sup>CO ( $p_{CO} < 1$  Torr) and formation of nickel(I) monocarbonyls (dotted line corresponds to <sup>13</sup>CO adsorption). (c) FTIR spectra (ambient temperature) of <sup>12</sup>CO adsorption on (1) thermally activated NiZSM-5, after reduction in CO (620 K) and subsequent evacuation at (2) 320 K and (3) 350 K leading finally to formation of sole monocarbonyl species of nickel(I).

### 3.2 Binding of CO to Ni(I) sites

The planar structure of the parent intrazeolite  $\text{Ni}^{\text{I}}\{\text{O}(\text{Si},\text{Al})\}_4$  sites is comparable to the coordination environment of nickel in the homogeneous complexes with tetra-dentate supporting macroligands<sup>55</sup> and nickel enzymes.<sup>21</sup> Thus, similar EPR spectra of the Ni(I) centers have also been observed. Favorable spatial and energetic accessibility of the nickel orbitals, controlled by weak oxygen donor ligands of the zeolite matrix, makes capture of CO molecules quite easy. Indeed, adsorption of  $^{12}\text{CO}$  at 298 K (under the pressure below 1 Torr) on the reduced  $\text{Ni}^{\text{I}}\text{ZSM-5}$  sample led to development of a new well resolved orthorhombic EPR signal shown in Figure 1b, together with its computer simulation (green line). The obtained  $g$  tensor values are equal to  $g_{xx} = 2.018$ ,  $g_{yy} = 2.380$ ,  $g_{zz} = 2.436$ . Analogous experiment with isotopically labeled  $^{13}\text{CO}$  ( $I = 1/2$ , 90%) did not lead to appearance of any resolved superhyperfine structure due to  $^{13}\text{C}$  nuclear spin, and a merely appreciable line broadening indicated that the spin density is essentially retained on the nickel center upon CO attachment. This point was further elucidated by means of HYSCORE spectroscopy (*vide infra*). The corresponding IR spectrum (Figure 1c) recorded in similar conditions revealed formation of an intense band at  $\nu_{\text{CO}} = 2109 \text{ cm}^{-1}$  characteristic of the C–O stretching vibration (the accompanying bands at 2136 and 2091  $\text{cm}^{-1}$  are due to the dicarbonyl species).<sup>56</sup> A bathochromic shift of this band  $\Delta\nu = -34 \text{ cm}^{-1}$  with respect to the gas-phase indicates domination of the  $\pi$  back-donation over the  $\sigma$  donation effects, discussed below in more detail. Based on the  $g$  tensor and  $\nu_{\text{CO}}$  signatures, the observed adduct can be assigned to the covalently bound monocarbonyl nickel(I) species.<sup>13,56,57</sup>

**Table 1.** Experimental and DFT calculated spectroscopic parameters (frequency of the CO vibration,  $\nu_{\text{CO}}$ ,  $\mathbf{g}$  tensor, hyperfine splitting,  $\mathbf{A}$ , quadrupole tensor,  $\mathbf{Q}$  ( $e^2Qq/h$ ,  $\eta$ ), and orientation of the principal axes of the  $\mathbf{A}$  ( $^{13}\text{C}$ ) tensor with respect to the  $\mathbf{g}$  tensor coordinates for the nickel(I) monocarbonyl adducts in ZSM-5 zeolite.

spectroscopic parameters	experimental values			DFT-calculated values		
$\nu_{\text{CO}} / \text{cm}^{-1}$	2109			2107		
$\mathbf{g}$ tensor						
$g_{xx}, g_{yy}, g_{zz}$	2.018 ± 0.001	2.380 ± 0.005	2.436 ± 0.005	2.016	2.224	2.433
$^{13}\text{C}$ hyperfine tensor						
$A_{xx}, A_{yy}, A_{zz} / \text{MHz}$	+1.0 ± 0.3	-3.6 ± 0.9	-1.6 ± 0.3	+5.9	-9.4	-4.9
Euler angles <sup>a)</sup>						
( $^{13}\text{C}$ ) $\mathbf{A}$ tensor $\alpha, \beta, \gamma / \text{deg}$	0	84	0	0	80	-2

<sup>a)</sup> Euler rotations are defined assuming first rotation by  $\alpha$  around  $z$  axis, second rotation by  $\beta$  around  $y'$  axis, and finally third rotation by  $\gamma$  around  $z''$  axis.

The observed  $\mathbf{g}$  tensor anisotropy and symmetry of the EPR signal can be used for assigning the coordination mode of the  $\{\text{Ni}^{\text{I}}\text{-CO}\}$  monocarbonyl. As already mentioned, it can assume one of the generic **T** or **Y** conformations known from bioinorganic complexes, where the nickel(I) core is three-coordinated.<sup>6,21,24</sup> As shown earlier the  $\mathbf{g}$  tensor is sensitive to the conformation type and the resulting ground state,<sup>24</sup> which allows for a clear-cut assignment of the observed  $\{\text{Ni}^{\text{I}}\text{-CO}\}$

adduct in ZSM-5 to the **T** conformation with the predominant  $3d_{xz}$  SOMO, consistent with the observed sequence  $g_{zz} > g_{yy} \gg g_{xx}$  of the  $g$  values (Table 1).

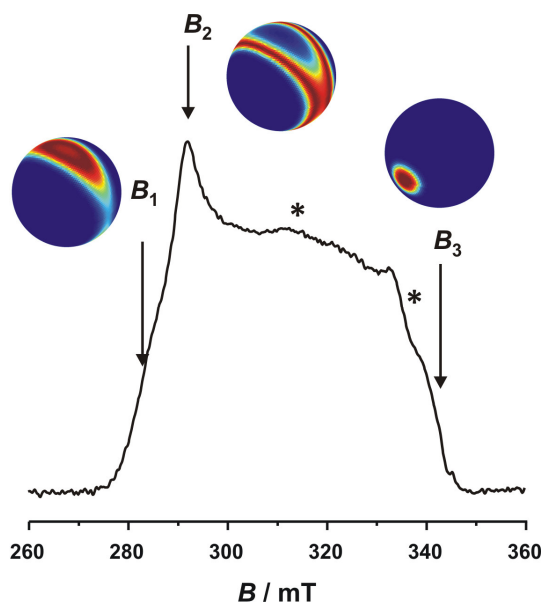


**Figure 2.** Echo-detected EPR spectrum of  $\{\text{Ni}^{\text{I}}-^{12}\text{CO}\}$ ZSM-5 monocarbonyl adduct ( $\pi/2 = 16$  ns,  $\tau = 200$  ns,  $T = 10$  K). The arrows indicate the observer positions  $B_1$ ,  $B_2$ , and  $B_3$  at which HYSORE spectra were recorded, whereas the unit spheres show orientation selectivity calculated for the particular observer positions (red shadings indicate orientations on resonance with the microwave pulse, blue shadings off-resonance). The asterisks indicate weak features due to nickel(I) dicarbonyl species.

To determine the hyperfine splitting due to  $^{13}\text{CO}$ , unresolved in the simple CW-EPR experiments, and to ascertain the coordination environment of the  $\{\text{Ni}^{\text{I}}-\text{CO}\}$  magnetophore hosted in the ZSM-5 zeolite, a number of pulse EPR measurements were carried out. At first, an electron spin echo (ESE) detected EPR spectrum of the nickel(I) monocarbonyl was recorded



(Figure 2), the first derivative of which closely resembles the corresponding CW-EPR spectrum shown in Figure 1b. The weak features indicated by the asterisks are due to the residual nickel(I) dicarbonyl species, as revealed in separate CW-EPR experiments, recorded with increasing CO pressures (spectra not shown). The ESE spectrum was used for selection of the magnetic field observer positions ( $B_1$ ,  $B_2$ , and  $B_3$ ) corresponding to the principal orientations of the  $g$  tensor at which the HYSCORE experiments were next carried out. Taking the  $g$  tensor values derived from computer simulation of the powder CW-EPR spectra (Table 1), the computed orientation selection on the unit sphere (Figure 2) shows that at the field position  $B_3$ , only the species with the  $g_{xx}$  axis oriented along or close to the magnetic field contribute to the measurement. This orientation selective excitation allows to determine the magnetic interactions missing in CW-EPR (hyperfine and quadrupole couplings), with respect to the  $g$  tensor coordinate system. The unit sphere calculated for the observer position  $B_2$ , corresponding to the  $g_{yy}$  axis, shows that many orientations in the  $g_{yy}$ - $g_{zz}$  plane of the  $\{\text{Ni}^{\text{I}}\text{-CO}\}$  species are in resonance with the microwave pulse, and jointly contribute to the measurement. Even though that the  $B_1$  orientation seems to be more selective than the  $B_2$  one, the highest intensity of the echo obtained for the latter position favored performing the HYSCORE experiments at the magnetic field set at  $B_2$ . Note that due to spin diffusion associated to the large linewidths the experiment is orientation less selective than implied by somehow idealized picture shown in Figure 2.

In HYSCORE experiments a correlation of nuclear frequencies in one electron spin ( $m_S$ ) manifold with nuclear frequencies in the other manifold is created by means of a mixing  $\pi$  pulse. In the particular case of the  $\{\text{Ni}^{\text{I}}\text{-}^{13}\text{CO}\}$ ZSM-5 paramagnets, the hyperfine interactions are expected for  $^{13}\text{C}$  nuclei ( $I = 1/2$ ,  $\nu_{\text{C}} = 3.748$  MHz) of the adsorbed CO and  $^{27}\text{Al}$  ( $I = 5/2$ ,  $\nu_{\text{Al}} = 3.886$  MHz) atoms of the alumino-silicious framework (zeolite). Given the similarity of the

Larmor frequencies (calculated for 350 mT) of these two nuclei, the HYSCORE spectra were recorded for both  $\{\text{Ni}^{\text{I}}-^{12}\text{CO}\}$ ZSM-5 and  $\{\text{Ni}^{\text{I}}-^{13}\text{CO}\}$ ZSM-5 systems.

In the case of the  $\{^{12}\text{CO}-\text{Ni}^{\text{I}}\}$  isotopomer, the HYSCORE spectrum taken at a field position corresponding to B1 (292.0 mT) (Figure 3a and 3d) shows an intense peak on the (+,+) quadrant diagonal at  $(\nu_{\text{Al}}, \nu_{\text{Al}})$  amenable to the interaction with at least one  $^{27}\text{Al}$  nucleus. Recording the spectrum at position B2 reveals the presence of multiple diagonal peaks (Figure 3d) with considerable shift with respect to the  $^{27}\text{Al}$  nuclear Larmor frequency. This can be explained considering a fairly large quadrupole interaction. Literature values, ranging from 11 to 16 MHz, have been reported for  $^{27}\text{Al}$  in ZSM-5 and similar systems (faujasite, mordenite)<sup>58,59</sup>. DFT computed values (vide infra) predict a quadrupole coupling of 13 MHz in line with these results. The poor resolution of the HYSCORE spectra and the large number of parameters (9) that concur to determine the HYSCORE spectrum of  $^{27}\text{Al}$  hamper the experimental determination of the full interacting tensors, however simulation of the HYSCORE spectra carried out using the DFT predicted values for the  $^{27}\text{Al}$  interactions (Table 1) provide an acceptable reproduction of the main spectral features (Supporting Information). This in turn provides a valuable background for development of a confident model of the investigated adduct and subsequent in-depth interpretation of the data with help of much more wide-ranging DFT results.

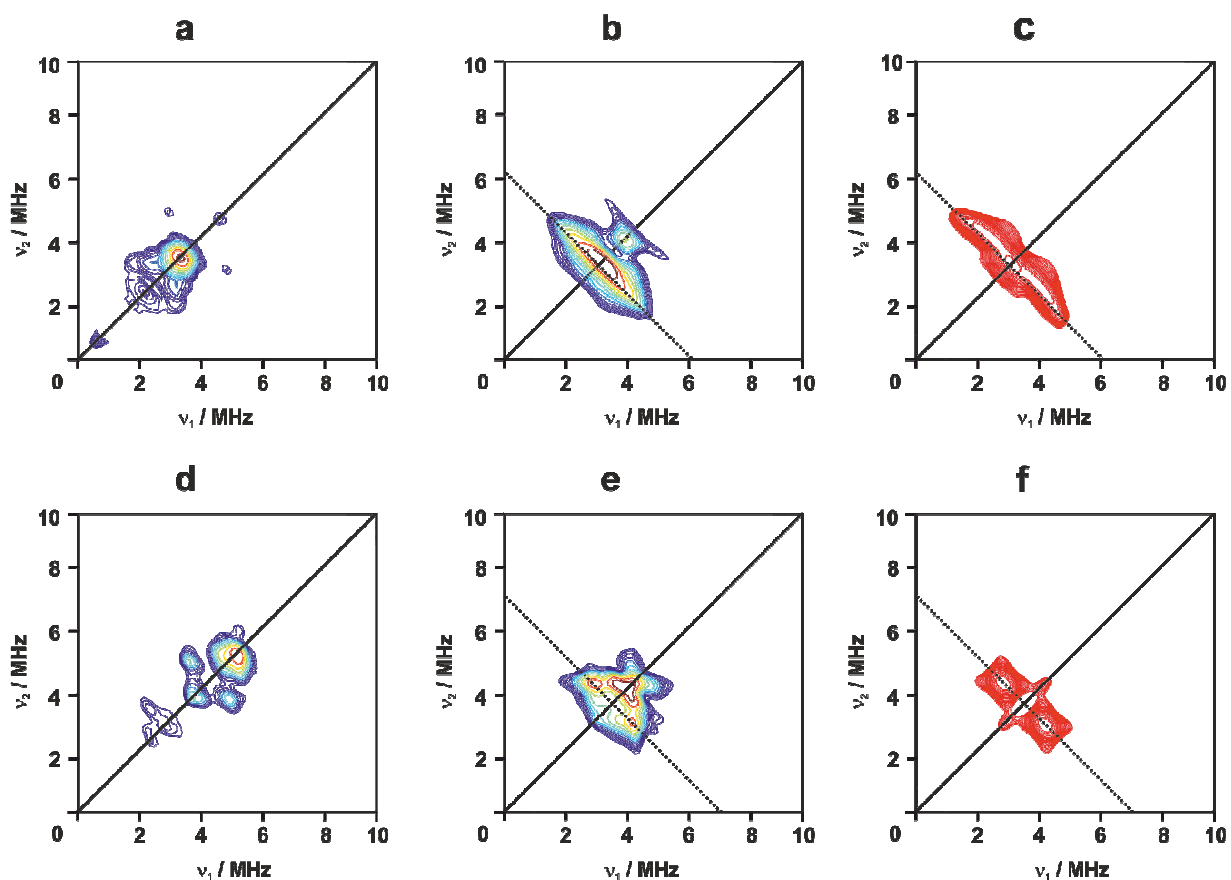


**Figure 3.** HYSORE spectra of the  $\{\text{Ni}^1\text{-}^{13}\text{CO}\}$ ZSM-5 adducts taken at the observer positions (a)  $B_2$  and (d)  $B_3$  at 10 K with  $\tau = 112$  ns and 128 ns, and 0.75 kHz repetition rate. Simulated HYSORE patterns (b, e) (red contour – simulation, black contour – experiment) arising from the hyperfine interaction due to one  $^{13}\text{C}$  ( $I = 1/2$ ) nucleus and hyperfine and quadrupole interaction due to one  $^{27}\text{Al}$  ( $I = 5/2$ ) nucleus, (c, f) simulated component signal due to the contribution of the sole  $^{13}\text{C}$  nucleus. Dotted lines indicate Larmor frequency of  $^{13}\text{C}$  for each magnetic field value.

When  $^{13}\text{CO}$  ( $I = 1/2$ , 90%) was used, a new ridge centered at the  $^{13}\text{C}$  nuclear Larmor frequency was observed upon setting the magnetic field at the position  $B_2$ , which was not present in the case

when  $^{12}\text{C}$ O was used (Figure 3a). Recording the spectrum at the magnetic field equivalent to the  $g_{xx}$  component (the position  $B_3$  in Figure 2) led to a single crystal like spectrum (Figure 3e), characterized by two peaks centered at the Larmor frequency of  $^{13}\text{C}$ . These signals are unambiguously assigned to the superhyperfine interaction between the unpaired electron, localized on the Ni  $3d_{xz}$  orbital, and the  $^{13}\text{C}$  nucleus of the CO ligand. The maximum ridge extension of  $\approx 4$  MHz, measured parallel to one of the axes in the spectrum of Figure 3b, corresponds to the maximum hyperfine coupling ( $A_{\text{max}}$ ). Moreover, the  $^{13}\text{C}$  ridge is clearly shifted from the  $(\nu_C, \nu_C)$  value, revealing a substantial dipolar interaction. Simulation of the spectra at two different magnetic field settings (Figure 3b,e) allow for determining the full  $^{13}\text{C}$  hyperfine tensor, which is reported in Table 1. The individual patterns due to the contribution of a  $^{13}\text{C}$  nucleus are shown in Figure 3c,f. It should be noted that in the simulations the contributions of remote  $^{27}\text{Al}$  and  $^{13}\text{C}$  nuclei were neglected. This explains the slightly different shape in the experimental and simulated ridges.

The resulting  $^{13}\text{C}$  hyperfine tensor is highly dipolar in nature with the maximum coupling oriented along the “perpendicular”  $g_{yy}$  component (note almost  $\pi/2$  rotation of the  $A_{ii}$  and  $g_{ii}$  principal axes along the  $y$  direction, Table 1). Conventional decomposition of the  $A(^{13}\text{C})$  tensor ( $A = a_{\text{iso}}\mathbf{I} + \mathbf{T}$ ) leads to  $\mathbf{T} / \text{MHz} = [+2.4; -2.2; -0.2]$  and  $a_{\text{iso}} = -1.4$  MHz, in accordance with the positive principal value of the dipolar coupling for 2p orbitals and positive  $g_n$  value for  $^{13}\text{C}$  nucleus.<sup>60</sup> The negative isotropic constant is in agreement with the B3LYP calculations (Table 1), and its origin is well accounted for by an asymmetric  $\alpha$  and  $\beta$  electron density flow within the  $\{\text{Ni}^{\text{I}}\text{-CO}\}$  moiety, discussed below in detail. The very small values of the  $^{13}\text{C}$  hyperfine parameters suggest either a distal ligand-metal coordination (for instance inverted Ni–OC bond) or minute delocalization of the spin density onto the CO ligand. Since the  $A(^{13}\text{C})$  tensor exhibits

a predominant dipolar through space nature, we verified the self-consistency of the obtained HYSCORE spectra simulation with the proposed molecular model of the  $\{\text{Ni}^{\text{I}}\text{-CO}\}$  adduct, using the estimation of the dipolar coupling based on a separate (diffuse) dipole approximation.<sup>61</sup> In this approach the maximal hyperfine splitting,  $A_{\text{max}}$ , can be associated with the Ni-C bond length,  $R$ , using the following formula:

$$A_{\text{max}} = g\mu_B g_n \mu_n \left[ \frac{2R^2 - r^2}{2(R^2 + r^2)^{5/2}} + \frac{(R - r)^3 + (R + r)^3}{2(R + r)^3 (R - r)^3} \right], \quad (2)$$

where  $r$  indicates the most probable distance of the unpaired electron from the nickel nucleus. For 3d states it can be approximated as  $6a_0/Z^*$  ( $a_0 = 0.52918 \text{ \AA}$ ), where the effective atomic number was calculated using the Slater rules:  $Z^* = 7.2$  (for  $3d^9$  electron configuration). Taking  $R = 1.77 \text{ \AA}$  obtained from the DFT geometry optimization (see below) and uncertainty of the  $r$  value of  $\pm 0.1 \text{ \AA}$ , by substituting numerical values  $A_{\text{max}} = 4.9 \pm 0.8 \text{ MHz}$  was obtained, in reasonable agreement with the extent of the  $^{13}\text{C}$  ridge (Figure 3c,f, Table 1), taking into account inherent approximations of both approaches.

The very small spin density transfer toward the CO ligand is at first glance surprising, in view of a pronounced metal to ligand  $\pi$  back-donation revealed by the sizable ( $\Delta\nu = -34 \text{ cm}^{-1}$ ) red shift of the CO stretching frequency. In order to clarify this conundrum, and to develop a detailed self-consistent description of the electronic and molecular structure of the monocarbonyl complex, corroborative DFT calculations were carried out.

### 3.3 Electronic structure and binding mechanism of $\{\text{Ni}^{\text{I}}\text{-CO}\}$

DFT calculations revealed that the  $\{\text{Ni}^{\text{I}}\text{-CO}\}\text{M7}$  adduct exhibits a moderately strong  $\eta^1$  binding of the CO molecule (Figure 4a) with  $\Delta E_{\text{int}} = -163 \text{ kJ/mol}$ . The planar three-fold

coordination around the nickel center is featured by the top-on ligated CO moiety, with the distance to the metal center of 1.748 Å, and two longer Ni–O<sub>(Al)</sub> bonds with the zeolite framework equal to 2.043 Å and 1.926 Å. The C–O bond length is elongated to 1.155 Å upon bonding with respect to the free CO<sub>(g)</sub> molecule (1.140 Å), and the O<sub>(Al)</sub>–Ni–C angle of 166° nicely corroborates the **T** conformation deduced from the analysis of the experimental **g** tensor. Coordination of the carbon monoxide molecule occurs in an alterdesmic way (*i.e.* without preserving the total number of bonds), since one new bond to the CO ligand is formed at the expense of two broken Ni–O<sub>(Si)</sub> strained connections with the zeolite framework. Such adsorption mechanism results in a trigonal OC–Ni<sup>I</sup>–(O<sub>(Al)</sub>)<sub>2</sub> geometry and is typical of the constraint (entatic) environments such as enzyme prosthetic groups<sup>6,19,21</sup> or intrazeolite hosting sites.<sup>2</sup> Binding via an aluminum tetrahedron to the zeolite framework explains the observed HYSORE patterns due to <sup>27</sup>Al quadrupole interaction and a large value of the  $e^2qQ/h$  parameter (Table 1).

The revealed **T** conformation of the monocarbonyl adduct gives rise to the spin density distribution essentially confined to the nickel core (Figure 4b). The orientation of the principal axes of the **g** tensor with respect to the molecular framework of the {Ni<sup>I</sup>–CO}M7 complex is shown in Figure 4c,d. Both  $g_{xx}$  and  $g_{zz}$  axes are localized in the O<sub>(Al)</sub>–Ni–O<sub>(Al)</sub> plane that incorporates the CO ligand, with the  $g_{zz}$  axis aligned nearly parallel to the C–O bond. The  $g_{xx}$  axis is slightly tilted outward the Ni–O<sub>(Al)</sub> bond (18°). Alignment of the  $g_{yy}$  axis (Figure 4d) is perpendicular to the O–Ni–O plane. In agreement with the low local symmetry of the CO–Ni<sup>I</sup>–(O<sub>(Al)</sub>)<sub>2</sub> unit (approximately the C<sub>s</sub> point group giving rise to a monoclinic EPR spectrum), the principal axes of the <sup>13</sup>C hyperfine tensor are non-collinear with the **g** tensor axes in the *xz* plane. They are rotated nearly about  $\beta = 90^\circ$  along the *y* direction (Table 1).

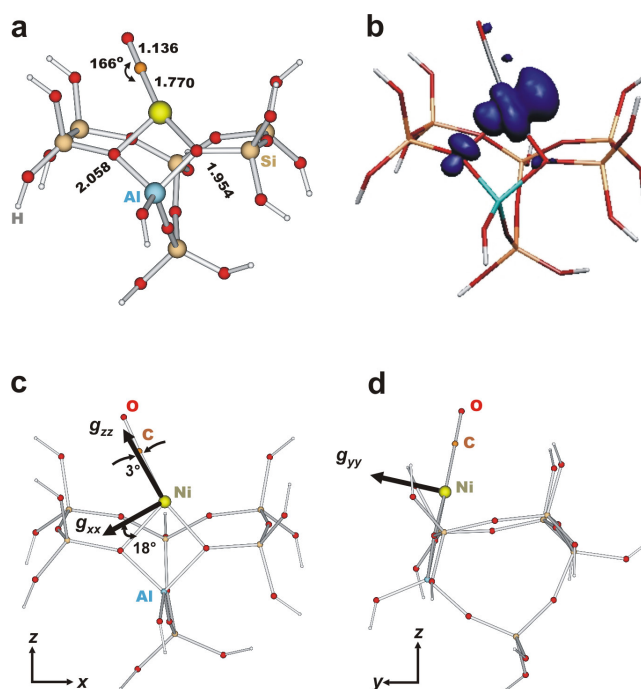


**Figure 4.** (a) DFT optimized structure of the  $\{\text{Ni}^{\text{I}}\text{-CO}\}\mathbf{M7}$  cluster, (b) the corresponding spin density contour, and (c, d) orientation of the principal axes of the  $g$  tensor with respect to the molecular framework. Bond lengths are given in Angstroms, and angles in degrees.

The intimate nature of the CO binding to the intrazeolite Ni(I) sites was examined in more detail with the help of a frontier molecular orbital (FMO) interaction diagram of the constituting molecular fragments. The latter are defined by the carbon monoxide ligand,  $[\text{CO}]_{\text{frag}}$ , a tetra-coordinate nickel(I) site hosted in the ZSM-5,  $[\text{Ni}^{\text{I}}_{4\text{c}}\mathbf{M7}]_{\text{frag}}$ , and a bidentate nickel site in a virtual entatic state,  $[\text{Ni}^{\text{I}}_{2\text{c}}\mathbf{M7}]_{\text{frag}}$ , corresponding to the actual coordination environment of the nickel moiety in the  $\{\text{Ni}^{\text{I}}\text{-CO}\}\mathbf{M7}$  adduct with the removed CO ligand (*vide infra*). This procedure has been justified by us earlier while resolving the electronic structure of the nickel-superoxo adducts.<sup>27</sup> Since upon interaction with CO the coordination state of nickel(I) changes dramatically from the planar four-fold to the T-shaped trigonal one, the  $\{\text{Ni}^{\text{I}}\text{-CO}\}\mathbf{M7}$  energy levels were correlated directly with the corresponding energy levels of the  $[\text{Ni}^{\text{I}}_{2\text{c}}\mathbf{M7}]_{\text{frag}}$  pro-

adduct, and not to the parent tetra-coordinated  $\text{Ni}^{\text{I}}_{4\text{c}}\mathbf{M7}$  center. In such approach, the interaction between CO and  $\text{Ni}^{\text{I}}$  can be factorized into two virtual steps involving an intermediate entatatic  $[\text{Ni}^{\text{I}}_{2\text{c}}\mathbf{M7}]_{\text{frag}}$  pro-adduct of the geometry apt for direct binding of the impending CO molecule. Such three-fragment approach leads to a more transparent picture of the CO bonding, reducing a complicated mixing of too many orbitals to few key interactions between the meaningful FMO. The ensuing orbital overlap correlation diagram of the  $\pi(2\text{p})$  and  $\sigma$  states of the carbon monoxide ligand with the 3d states of the  $[\text{Ni}^{\text{I}}_{2\text{c}}\mathbf{M7}]_{\text{frag}}$  fragment referenced to the parent  $\text{Ni}^{\text{I}}_{4\text{c}}\mathbf{M7}$  cluster is shown in Figure 5.

In the  $[\text{Ni}^{\text{I}}_{2\text{c}}\mathbf{M7}]_{\text{frag}}$  pro-adduct state, the change in the nickel coordination results in a significant alteration of the energy of the nickel-based 3d orbitals (Figure 5). In particular, the position of the **146**( $3d_{yz}$ ) level of the  $\text{Ni}^{\text{I}}\mathbf{M7}$  cluster drops by 1.3 eV, making it energetically more accessible for interaction with the CO out-of-plane **5**( $\pi_y(2p_y)$ ) orbital, whereas that of **147**( $3d_{xz}$ ) one, of the same symmetry as the CO in-plane **6**( $\pi_x(2p_x)$ ) state, is almost unchanged. Essentially, the binding of CO results from the  $\pi$  overlap between low-laying  $\pi(2\text{p})$  CO states with the symmetry adopted  $3d_{xz}$  and  $3d_{yz}$  orbitals of nickel. It is further enhanced by small contribution due to the  $\sigma$  overlap between **7**( $\sigma(2\text{p}+2\text{s})$ ) and one of the lobes of the in-plane **149**( $3d_{xz}$ ) orbital, produced by the unusual T-shape geometry of the CO–Ni–( $\text{O}_{(\text{Al})}$ )<sub>2</sub> unit. The low-laying **109** $\alpha$  and **107** $\alpha$ , **108** $\beta$  and **107** $\beta$  bonding spinorbitals have their antibonding **158** $\alpha$  and **157** $\alpha$ , **158** $\beta$  and **157** $\beta$  counterparts that contribute to the magnetic couplings responsible for the pronounced *g* tensor anisotropy, discussed below in more detail.



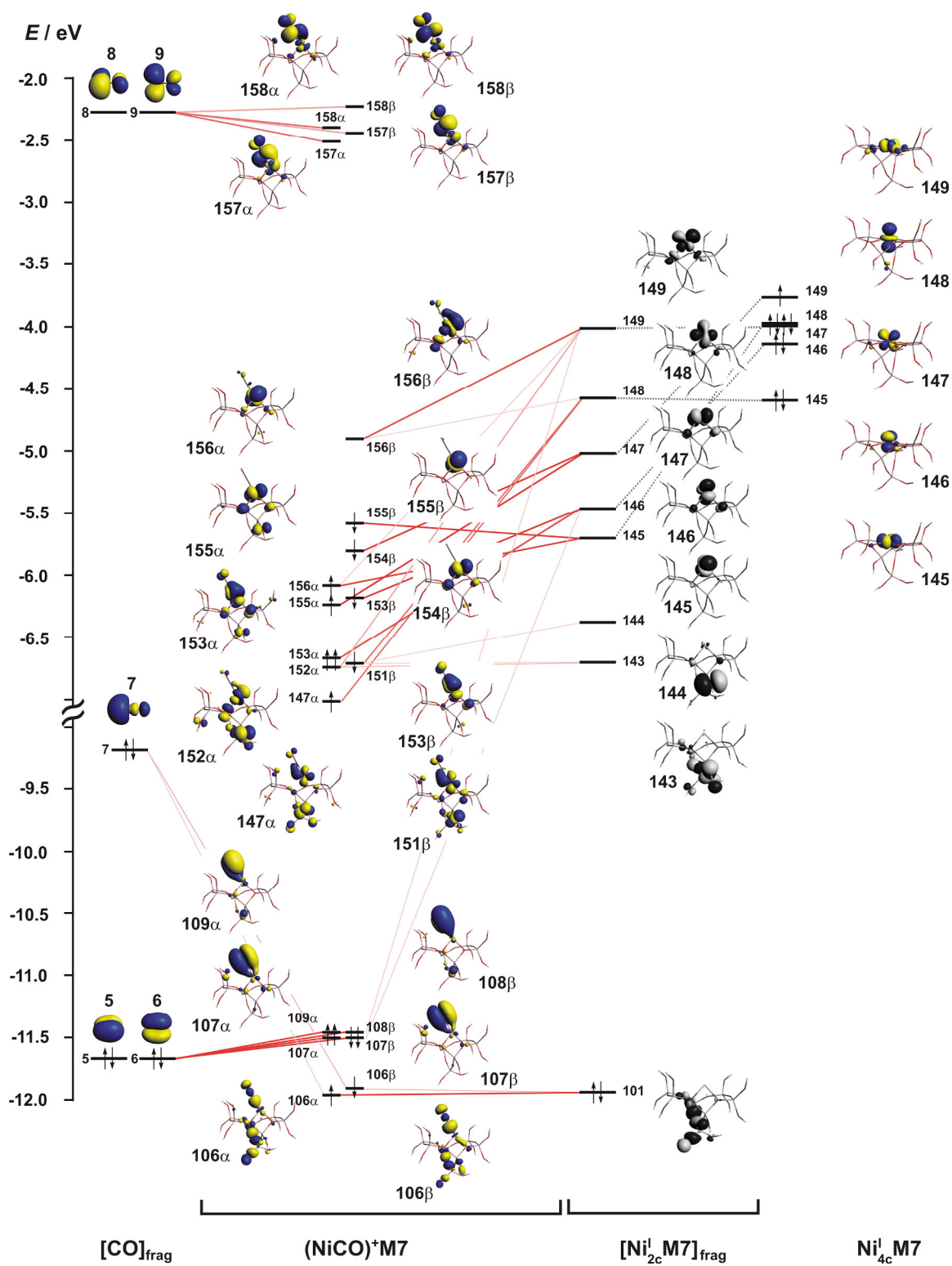


**Figure 5.** The Kohn-Sham orbital interaction diagram for the  $\{\text{Ni}^{\text{I}}-\text{CO}\}\text{M7}$  model complex.

The energy levels of the bonding and antibonding  $\pi(2p)$  CO orbitals define the low and high-energy boundaries encompassing the 3d nickel-based **145 – 149** states of the  $[\text{Ni}^{\text{I}}_{2\text{c}}\text{M7}]_{\text{frag}}$  pro-adduct. Those states, being essentially nonbonding with respect to the zeolite framework, generally remain also nonbonding in the CO- $\text{Ni}^{\text{I}}\text{M7}$  adduct. They are yet modulated by tiny contributions coming from the  $\pi^*_x$  and  $\pi^*_y$  states of CO, giving rise to **152 $\alpha$**  and **156 $\beta$** , **153 $\alpha$**  and **153 $\beta$**  MOs, respectively. Thus, the interaction of the **145 – 149** 3d states with the corresponding CO orbitals results in a strong spin-polarization, reflected by the pronounced shift of the  $\alpha$  and  $\beta$  spin manifolds of the  $\text{Ni}^{\text{I}}\text{-COM7}$  species, and the changes in their energy ordering (compare the occupied **152 $\alpha$**  and the virtual **156 $\beta$**  states of the same symmetry Figure 5). The singly occupied **152 $\alpha$**  MO exhibits little delocalization on the CO moiety, which nicely explains the lack of  $^{13}\text{C}$  hyperfine splitting in the CW-EPR spectra (Figure 1b, dotted line). The residual spin density seen in Figure 4b accounts well for the very weak hyperfine interaction detected in the HYSORE experiments (see above). Although the **147 – 156** orbitals of the  $\text{Ni}^{\text{I}}\text{-COM7}$  adduct do not contribute directly to the binding of CO to the zeolite nickel(I) sites, they are of fundamental importance for explaining the experimentally observed increase of the  $\mathbf{g}$  tensor anisotropy with respect to the parent  $\text{Ni}^{\text{I}}$  sites (Figure 1a,b), explained below thoroughly.

### 3.4 DFT account of spectroscopic features of $\{\text{Ni}^{\text{I}}\text{-CO}\}$

According to the partitioning scheme implied by the scalar Pauli Hamiltonian approach,<sup>52</sup> the components of the experimental  $\mathbf{g}$  tensor ( $g_{ii} = g_e + \Delta g_{ii}$ ) can be rationalized in terms of the individual MO contributions to the particular  $g_{ii}$  values:  $\Delta g_{ij} = \Delta g^{\text{rel}}_{ij} + \Delta g^{\text{d}}_{ij} + \Delta g^{\text{p}}_{ij}$ , where  $\Delta g^{\text{rel}}_{st}$  combines scalar relativistic corrections, whereas the terms  $\Delta g^{\text{d}}_{st}$  and  $\Delta g^{\text{p}}_{st}$  stand for dia- and paramagnetic contributions to  $\Delta \mathbf{g}$ , respectively. The paramagnetic term ( $\Delta g^{\text{p}}_{st}$ ) dominates the

deviation of the  $g$  tensor elements from the free electron value. It contains the contributions due to a frozen core ( $\Delta g_{st}^{p,\text{core}}$ ), a magnetic field-induced coupling between the occupied orbitals ( $\Delta g_{st}^{p,\text{occ-occ}}$ ), and the occupied and the virtual magnetic orbitals ( $\Delta g_{st}^{p,\text{occ-virt}}$ ). It has been shown that  $\Delta g_{ij}^{p,\text{occ-virt}}$  dominates the paramagnetic term (and the total  $\Delta g_{ii}$  shift) for transition metal complexes,<sup>52</sup> including nickel(I) adducts.<sup>24,27</sup> Therefore, while discussing the molecular nature of the  $g$  tensor anisotropy for the Ni<sup>I</sup>-COM7 adduct, we may reasonably confine our description to this overwhelming term only.

The principal magnetic couplings to the  $g_{ij}$  components of the nickel(I) monocarbonyl adduct within the spin-unrestricted resolution are shown in Figure 6, along with the contours of the corresponding magnetic orbitals. Because of the  $C_1$  point symmetry of the Ni<sup>I</sup>-COM7 species all possible couplings specified by the following integrals are allowed:<sup>62</sup>

$$\Delta g_{ij}^{p,\text{occ-virt}} \propto \frac{1}{2c(\varepsilon_{\text{virt}}^\sigma - \varepsilon_{\text{occ}}^\sigma)} \langle \Psi_{\text{virt}}^\sigma | iL_{x,y,z} | \Psi_{\text{occ}}^\sigma \rangle, \quad (3)$$

where  $\Psi_{\text{occ}}$  and  $\Psi_{\text{virt}}$  represent the occupied and the virtual unperturbed Kohn-Sham orbitals, respectively,  $\varepsilon$  is one-electron energy,  $L$  is the orbital momentum operator, whereas  $\sigma$  stands for  $\alpha$  or  $\beta$  spin. To simplify the diagram, only the most important contributions (above 15% of the  $\Delta g_{\text{iso}}$  value) are shown. For the sake of further discussion the  $\Psi_{\text{occ}}$  and  $\Psi_{\text{virt}}$  states can be classified as the metal-based and ligand-based spinorbitals.

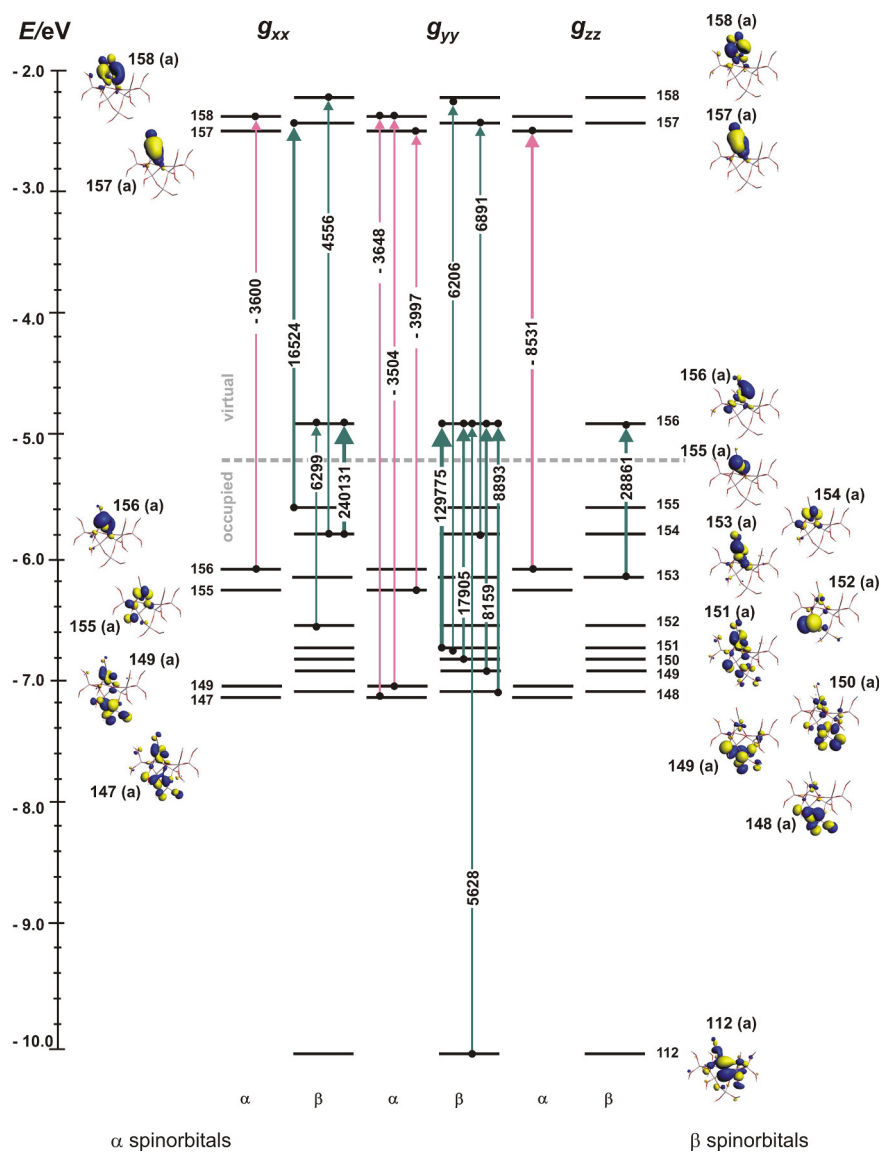


**Figure 6.** Kohn-Sham orbital diagram for the most important paramagnetic contributions to the  $g$  tensor components of the Ni<sup>I</sup>-COM7 cluster in the spin-unrestricted BP/TZP scalar relativistic calculations based on the Pauli Hamiltonian. The magnetic field-induced couplings (transitions) are indicated with arrows, whereas the values of the corresponding contributions to  $\Delta g_{ii}$  ( $> 10\%$ ) are given in ppm.

The small positive shift of the  $g_{xx}$  component with respect to  $g_e$  value can be explained by a single metal-ligand positive coupling defined by the  $\beta\text{-153}a(d_{yz}+\pi_{y,\text{CO}}^*) \leftrightarrow \beta\text{-156}a(d_{xz}+\pi_{x,\text{CO}}^*)$  transition induced by the magnetic-field, which is attenuated by the negative  $\alpha\text{-156}a(d_y^2) \leftrightarrow \alpha\text{-157}a(d_{yz}+\pi_{y,\text{CO}}^*)$  component. Note that the  $\beta\text{-156}a(d_{xz}+\pi_{x,\text{CO}}^*)$  MO is an empty counterpart of the  $\alpha\text{-152}a$  SOMO state, and that it is mostly involved in all  $g_{ii}$  components.

The high anisotropy of the  $g$  tensor, reflected by large positive shift of the  $g_{zz}$  ( $\Delta g_{zz} = 0.434$ ) value, results mainly from the dominant  $\beta\text{-154}a(d_x^2 - y^2) \leftrightarrow \beta\text{-156}a(d_{xz}+\pi_{x,\text{CO}}^*)$  coupling. This major contribution is associated with its specific metal-to-metal character, small energy separation of the involved states, and large spin-orbit coupling constant ( $\xi = 605 \text{ cm}^{-1}$ ) of the nickel(I) core. It is additionally reinforced by three weaker  $\beta\text{-152}a(d_{xz}+L_{zeol}) \leftrightarrow \beta\text{-156}a(d_{xz}+\pi_{x,\text{CO}}^*)$ ,  $\beta\text{-154}a(d_x^2 - y^2) \leftrightarrow \beta\text{-158}a(d_{xz}-\pi_{x,\text{CO}}^*)$ , and  $\beta\text{-155}a(d_y^2) \leftrightarrow \beta\text{-157}a(d_{yz}-\pi_{y,\text{CO}}^*)$  magnetic transitions: All of them exhibit mostly a metal-to-ligand character, and by involving energetically strongly separated states are of less importance.

In the case of the  $g_{yy}$  component, the number of transitions increases to seven (Figure 6), leading to a complex coupling scheme. However, the most important  $\beta\text{-151}a(d_{xz}+d_{yz}+\pi_{x,\text{CO}}^*) \leftrightarrow \beta\text{-156}a(d_{xz}+\pi_{x,\text{CO}}^*)$  transition along with the combinations of the  $\beta\text{-150}a$ ,  $\beta\text{-149}a$ , and  $\beta\text{-148}a$  magnetic orbitals, all coupled to  $\beta\text{-SOMO } 156a(d_{xz}+\pi_{x,\text{CO}}^*)$ , exhibit a strong metal-to-metal character, and therefore, give rise to the large  $\Delta g_{yy}$  shift. It is further enhanced by the  $\beta\text{-151}a(d_{xz}+d_{yz}+\pi_{x,\text{CO}}^*) \leftrightarrow \beta\text{-158}a(d_{xz}-\pi_{x,\text{CO}}^*)$  and  $\beta\text{-154}a(d_x^2 - y^2) \leftrightarrow \beta\text{-157}a(d_{yz}-\pi_{y,\text{CO}}^*)$  transitions involving antibonding  $\pi^*$  states of the CO ligand. Consequently, the resultant coupling scheme provides a detailed rigorous molecular rationale for the  $g_{zz} > g_{yy} \gg g_{xx}$  sequence that is actually observed in the CW-EPR experiment, with the unprecedented accuracy.

The already mentioned red shift  $\Delta\nu = -34 \text{ cm}^{-1}$  of the C–O stretching frequency with respect to the gas-phase carbon monoxide (Figure 1c) can be accounted for by the electron population analysis obtained from DFT calculations. It was found that upon ligation the CO molecule acquires a negative charge ( $q_{\text{CO}} = -0.04$ ), whereas the Ni center becomes oxidized ( $\Delta q_{\text{Ni}} = +0.05$ ) with respect to the bare  $\text{Ni}^{\text{I}}\mathbf{M7}$  site. The partial charge redistribution within the  $\{\text{CO-Ni}^{\text{I}}\}$  unit arises from the balance between the ligand-to-metal (donation) and the metal-to-ligand (back-donation) flows of the electron density between the interacting moieties. In classic description of the electron repartition for metal carbonyl adducts,<sup>63</sup>  $\sigma$  donation results in a slight increase of the CO stretching frequency (since the  $\sigma$  lone pair of CO is partially antibonding), which can be enhanced further by electrostatic interactions.<sup>15</sup> The  $\pi$  back-donation effect provides the mechanism of decreasing the stretching frequency with respect to that of gas-phase CO. due to partial population of the  $\pi^*(2p)$  orbitals. This delicate balance between the donation and the back-donation effects was quantified in this study by means of the ETS-NOCV analysis, and the specific charge and spin flow channels were identified and arranged in terms of their energetic relevance. Within the assumed decomposition scheme into the  $[\text{CO}]_{\text{frag}}$  and  $[\text{Ni}^{\text{I}}_{2\text{c}}\mathbf{M7}]_{\text{frag}}$  fragments, the main contributions ( $|v_{\mathbf{k}}| > 0.1$ ) to the  $\alpha$  and  $\beta$  electron and spin density flows are shown in Figure 7, along with the corresponding energy values.

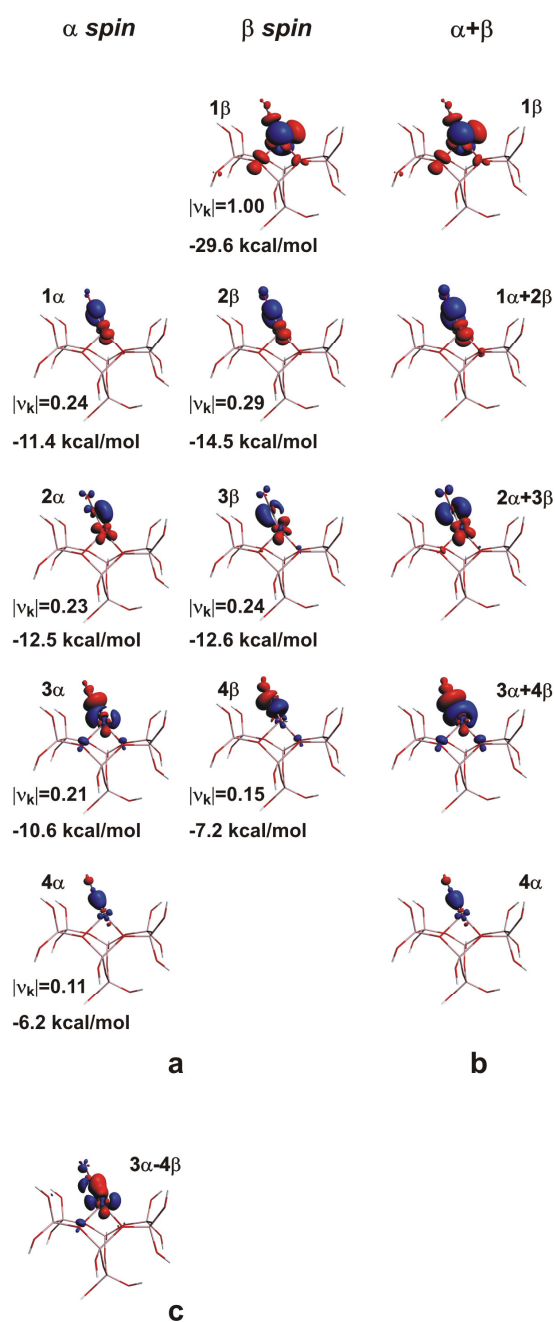


**Figure 7.** NOCV deformation density contours revealing electron density flow channels between interacting  $[\text{Ni}_{12c}\mathbf{M7}]_{\text{frag}}$  and  $[\text{CO}]_{\text{frag}}$  fragments (a) in spin unrestricted resolution, (b) total electron density ( $\alpha + \beta$ ) contours and (c) spin density ( $\alpha - \beta$ ) contour for  $3\alpha + 4\beta$  channel. The corresponding values indicate interaction energies characteristic of the individual channels. Blue and red shading corresponds to gain and loss of the electron (spin) density, respectively.

Using the local symmetry arguments, the overlapping orbitals may be categorized into the  $\sigma$  and  $\pi$  channels. The  $\pi$  channels are formed by two pairs of the spinorbitals,  $1\alpha + 2\beta$  and  $2\alpha + 3\beta$ , involving two perpendicular  $\pi_y^*$  and  $\pi_x^*$  molecular orbitals of the CO ligand, respectively. Since both  $\alpha$  and  $\beta$  spin manifolds are equally involved herein, these channels can be identified with the spinless charge transfer process. The  $\pi$  channel is involved in the back-donation charge transfer from  $3d_{yz}$  to  $\pi_y^*$  ( $1\alpha + 2\beta$ ) and from  $3d_{xz}$  to  $\pi_x^*$  ( $2\alpha + 3\beta$ ) orbitals. This flow is responsible for the lowering of the CO stretching frequency.

The  $\sigma$  donation channel is constituted by the  $3\alpha + 4\beta$  pair of the spinorbitals, giving rise to the cooperative charge transfer from the CO ligand to the 3d orbitals of nickel (mainly  $3d_{xz}$  and  $3d_z^2$ ), associated with a moderate energy gain ( $-17.8$  kcal/mol). This channel is slightly augmented by another  $\sigma$  channel ( $4\alpha$ ), yet of a very small energy ( $-6.2$  kcal/mol), operating only within the  $\alpha$  spin states (consistent thereby with a congruent spin and charge transfer), which leads to a very small spin density on the CO ligand. As a result, the sum of the individual contributions to the energy due to the orbital interaction along the  $\pi$  channel ( $-50$  kcal/mol) dominates the effects arising from the  $\sigma$ -channel ( $-24$  kcal/mol), which explains the observed distinct bathochromic CO stretching frequency shift.

The congruent rearrangement of the  $\beta$ -spin and charge, observed for the  $1\beta$  channel, can be interpreted as a relaxation process involving the  $3d_{xz}$  and  $3d_y^2$  nickel-based orbitals induced by CO ligation. The entatic  $[\text{Ni}_{2c}^I\mathbf{M7}]_{\text{frag}}$  reference fragment represents the state of enhanced energy, which upon interaction with CO not only allows for electron density redistribution within the  $\sigma$  and  $\pi$  channels, but also involves appropriate rearrangement of 3d levels (Figure 5), reflected by



one electron flip between 3d orbitals (*vide*  $|v_k| = 1$  for  $1\beta$ ), referred to as a metal core orbital relaxation process.

As a result, the applied ETS-NOCV analysis allowed for disentangling and quantification of the cooperative  $\sigma$  donation and  $\pi$  back-donation effects involved in the binding of CO to nickel(I). Indeed, the dominant contribution arises from the back-donation  $\pi$  channel of spinless charge transfer. This explains the position of the carbonyl band in the experimental IR spectrum (Figure 1c) and its bathochromic frequency shift with respect to the free CO molecule due to the net metal-to-ligand charge transfer. The spin density redistribution within the CO moiety operates mainly via  $4\alpha$  and  $3\alpha + 4\beta$   $\sigma$ -channels. Because of the significantly unequal contributions of the  $3\alpha$  and  $4\beta$  components, the resultant unbalanced spin flow (Figure 7c) gives rise to spin polarization of the carbon sp hybrid. On the contrary, the  $4\alpha$  channel allows for direct delocalization of the spin density onto the carbon 2s orbital. Yet, the polarization effect dominates that of the direct delocalization, which nicely rationalizes the negative sign of the isotropic constant  $a_{\text{iso}}(^{13}\text{C})$ , and consequently the convention of the signs for the  $A_{ii}(^{13}\text{C})$  components assumed in the HYSCORE simulations (Table 1). Being of opposite sign, those two effects lead to a very small total spin density flow within the  $\sigma$  channel. The dipolar  $T$  tensor, in turn, shows a noticeable rhombic symmetry. Accordingly, the dipolar  $^{13}\text{C}$  tensor can be decomposed into two axially symmetric contributions along the  $z$  and  $y$  directions as follows:  $[2.4; -2.2; -0.2] / \text{MHz} = [0.87; 0.87; -1.74] + [1.53; -3.06; 1.53]$ . The estimated proportion of  $2p_z$  and  $2p_y$  spin densities obtained from the principal values of both axial tensors ( $0.87/1.53 \approx 0.015/0.028$ ) agrees well with the Mulliken population analysis ( $\rho(2p_z) = -0.015$ ,  $\rho(2p_y) = -0.028$  and  $\rho(2p_x) = 0.000$ ).

Since upon CO ligation the unpaired electron relaxation process ( $1\beta$ ) is restricted to the nickel-based 3d orbitals only, and the main channels (one  $\sigma$  and two  $\pi$ ) of the electron density flow within the  $\{\text{Ni}^{\text{I}}\text{-CO}\}$  unit involve both  $\alpha$  and  $\beta$  spins in a similar way, the magnetophore part of the adduct is largely confined to the metal core (Figure 4b). All those effects provide the basis for molecular account of the observed IR and EPR parameters in terms of an incommensurate charge and spin flow.

#### 4. Conclusions

By means of combined use of CW-EPR, HYSCORE and IR spectroscopies, isotopically enriched carbon-13 and extensive multifaceted DFT molecular modeling it was demonstrated that interaction of carbon monoxide with  $\text{Ni}^{\text{I}}\text{ZSM-5}$  zeolite under low pressures leads to formation of a top-on monocarbonyl adduct of trigonal nickel(I), characterized by adsorption energy of  $\Delta E_{\text{int}} = -163$  kJ/mol. The EPR parameters with  $g_{zz} > g_{yy} \gg g_{xx} > g_e$ ,  $|A_{yy}| > |A_{zz}| > |A_{xx}|$  are characteristic of the **T**-conformation, resulting from alterdesmic ligation of CO accompanied by strong internal d-d relaxation of the metal core due to the joint  $\beta$ -spin and charge displacement between the  $3d_{xz}$  and  $3d_y^2$  orbitals. Based on the spectroscopic constraints ( $\nu_{\text{CO}}$  and  $\mathbf{g}$ ,  $\mathbf{A}({}^{13}\text{C})$ ,  $\mathbf{Q}({}^{27}\text{Al})$  tensors) refined by DFT modeling a comprehensive model of the electronic and magnetic structure of the adduct was developed. The spectroscopic parameters ( $g_{xx} = 2.018$ ,  $g_{yy} = 2.380$ ,  $g_{zz} = 2.436$ ,  $A_{xx} = +1.0$  MHz,  $A_{yy} = -3.6$  MHz,  $A_{zz} = -1.6$  MHz,  $e^2Qq/h = -13$  MHz,  $\eta = 0.9$ ) obtained by computer simulations of the EPR and HYSCORE spectra well reproduced by ZORS-SOMF/B3LYP calculations definitely validate the proposed the  $\eta^{\text{I}}$  **T**-structure. Detailed molecular nature of the  $\mathbf{g}$  tensor was rationalized in terms of the magnetic field-induced couplings of the magnetic molecular orbitals, using the scalar relativistic Pauli Hamiltonian

approximation. The disentangled charge and spin flows within the  $\{\text{Ni}^{\text{I}}\text{-CO}\}$  magnetophore along the orbital channels of  $\sigma$  and  $\pi$  symmetry were quantified by means of the ETS-NOCV method. The observed bathochromic shift of the C–O stretching frequency resulted from the dominant spinless  $\pi$  back-donation charge transfer ( $-50$  kcal/mol), while incongruent spin and charge transfer via the  $\sigma$  channel ( $-24$  kcal/mol) is responsible for the spin delocalization and spin polarization processes, giving rise to the observed disparity between the small spin density located on the CO ligand (EPR) and significantly larger charge transfer (IR).

### **Corresponding Author**

\* Piotr Pietrzyk, Faculty of Chemistry, Jagiellonian University, ul. Ingardena 3, 30-060 Krakow, POLAND, tel. +48 12 663 22 24, fax. +48 12 634 05 15, pietrzyk@chemia.uj.edu.pl

### **ACKNOWLEDGMENT**

Financial support for the research from the Ministry of Science and Higher Education (MNiSW) of Poland, grant no. Iuventus Plus IP2011 041871, is acknowledged. T. M. thanks the International PhD studies program within the MPD Program of Foundation for Polish Science co-financed by the EU Regional Development Fund for supporting his staying at the University of Torino. K. P. thanks for the postdoc position from the „Society – Environment –Technologies” project at the Jagiellonian University in the framework of the EU Social Fund. The calculations were carried out with the computer facilities of Academic Computing Centre CYFRONET-AGH under grant no. MNiSW/IBM\_BC\_HS21/UJ/092/2008. The research was carried out with the equipment purchased thanks to the financial support of the European Regional Development Fund in the framework of the Polish Innovation Economy Operational Program (contract no. POIG.02.01.00-12-023/08).

## REFERENCES

---

- (1) Costa, D.; Martra, G.; Che, M.; Manceron, L.; Kermarec, M. *J. Am. Chem. Soc.* **2002**, *124*, 7210-7217.
- (2) Aleksandrov, H. A.; Zdravkova, V. R.; Mihaylov, M. Y.; Petkov, P. St.; Vayssilov, G. N.; Hadjiivanov, K. I. *J. Phys. Chem. C* **2012**, *116*, 22823-22831.
- (3) Lupinetti, A. J.; Strauss, S. H.; Frenking, G. *Prog. Inorg. Chem.* **2001**, *49*, 1-112.
- (4) Zhou, M. F.; Andrews, L.; Bauschlicher, C. W.; *Chem. Rev.* **2001**, *101*, 1931-1962.
- (5) Mosqueda-Jiménez; B. I.; Jentys, A.; Seshan, K.; Lercher, J. A. *J. Catal.* **2003**, *218*, 375-385.
- (6) Craft, J. L.; Mandimutsira, B. S.; Fujita, K.; Riordan, C. G.; Brunold, T. C. *Inorg. Chem.* **2002**, *42*, 859-867.
- (7) Lepage, M.; Visser, T.; Soulimani, F.; Beale, A. M.; Iglesias-Juez, A.; Van Der Eerden, A. M. J.; Weckhuysen, B. M. *J. Phys. Chem. C* **2008**, *112*, 9394-9404.
- (8) Qi, G.; Xu, J.; Su, J.; Chen, J.; Wang, X.; Deng, F. *J. Am. Chem. Soc.*, **2013**, *135*, 6762-6765.
- (9) Wang, V. C.-C.; Can, M.; Pierce, E.; Ragsdale, S. W.; Armstrong, F. A. *J. Am. Chem. Soc.*, **2013**, *135*, 2198-2206.
- (10) Wang, W.-J.; Lin, H.-Y.; Chen, Y.-W. *J. Porous Mat.* **2005**, *12*, 5-12.

- 
- (11) Naknama, P.; Luengnaruemitchai, A.; Wongkasemjit, S.; Osuwan, S. *J. Power Sources* **2007**, *165*, 353-358.
- (12) Bernardo, P.; Algieri, C.; Barbieri, G.; Drioli, E. *Sep. Purif. Technol.* **2008**, *62*, 629-635.
- (13) Hadjiivanov, K.; Knözinger, H.; Mihaylov, M. *J. Phys. Chem. B* **2002**, *106*, 2618-2624.
- (14) Hadjiivanov, K. I.; Vayssilov, G. N. *Adv. Catal.* **2002**, *47*, 307-511.
- (15) Otero Arean, C.; Tsyganenko, A. A.; Escalona Platero, E.; Garrone, E.; Zecchina, A. *Angew. Chem. Int. Ed.* **1998**, *37*, 3161-3163.
- (16) Dorado, F.; de Lucas, A.; Garcia, P.B.; Romero, A.; Valverde, J.L.; Asencio, I. *Ind. Eng. Chem. Res.* **2005**, *44*, 8988-3996.
- (17) Mlinar, A. N.; Baur, G. B.; Bong, G. G.; Getsoian, A.; Bell, A. T. *J. Catal.* **2012**, *296*, 156-164.
- (18) Fakeeha, A. H.; Al-Fatesh, A. S.; Abasaheed, A. E. *Adv. Mater. Res.* **2012**, *550-553*, 325-328.
- (19) Harrop, T. C.; Mascharak, P. K. *Coord. Chem. Rev.* **2005**, *249*, 3007-3024.
- (20) Grochala, W. *Phys. Chem. Chem. Phys.* **2006**, *8*, 1340-1345.
- (21) Eckert, N. A.; Dinescu, A.; Cundari, T. R.; Holland, P. L. *Inorg. Chem.* **2005**, *44*, 7702-7704.
- (22) Frey, M. *Struct. Bonding* **1998**, *90*, 97-126.

- 
- (23) Bennett, B.; Lemon, B. J.; Peters, J. W. *Biochemistry* **2000**, *39*, 7455-7460.
- (24) Pietrzyk, P.; Podolska, K.; Sojka, Z. *Chem. Eur. J.* **2009**, *15*, 11802-11807.
- (25) Alvarez, S.; *Coord. Chem. Rev.* **1999**, *193-195*, 13-41.
- (26) Moncho, S.; Ujaque, G.; Lledos, A.; Espinet, P. *Chem. Eur. J.* **2008**, *14*, 8986-8994.
- (27) Pietrzyk, P.; Podolska, K.; Mazur, T.; Sojka, Z. *J. Am. Chem. Soc.* **2011**, *133*, 19931-19943.
- (28) Neese, F.; Munzarova, M. L. In *Calculation of NMR and EPR Parameters. Theory and Applications*; Kaupp, M., Bühl, M., Malkin, V. G., Eds.; Wiley-VCH: Weinheim, Germany, 2004, p. 21.
- (29) Pietrzyk, P.; Podolska, K.; Sojka, Z. *Electron Paramag. Reson.* **2013**, *23*, 264-311.
- (30) Stadler, C.; de Lacey, A. L.; Hernandez, B.; Fernandez, V. M.; Conesa, J. C. *Inorg. Chem.* **2002**, *41*, 4417-4423.
- (31) Ray, K.; Weyhermuller, T.; Neese, F.; Wieghardt, K. *Inorg. Chem.* **2005**, *44*, 5345-5360.
- (32) Sojka, Z.; Pietrzyk, P.; Martra, G.; Kermarec, M.; Che, M. *Catal. Today* **2006**, *115*, 154-161.
- (33) Pietrzyk, P.; Podolska, K.; Sojka, Z. *J. Phys. Chem. A* **2008**, *112*, 12208-12219.
- (34) Page, M. J.; Lu, W. Y.; Poulten, R. C.; Carter, E.; Algarra, A. G.; Kariuki, B. M.; MacGregor, S. A.; Mahon, M. F.; Cavell, K. J.; Murphy, D. M.; Whittlesey, M. K. *Chem. Eur. J.*, **2013**, *19*, 2158-2167.

- 
- (35) Spalek, T.; Pietrzyk, P.; Sojka, Z. *J. Chem. Inf. Model.* **2005**, *45*, 18-29.
- (36) Höfer, P.; Grupp, A.; Nebenfür, H.; Mehring, M. *Chem. Phys. Lett.* **1986**, *132*, 279-282.
- (37) (a) Stoll, S.; Schweiger, A. *J. Magn. Reson.* **2006**, *178*, 42-55, (b) Stoll, S.; Britt, R. D. *Phys. Chem. Chem. Phys.* **2009**, *11*, 6614-6625.
- (38) Mentzen, B. F.; Bergeret, G. *J. Phys. Chem. C* **2007**, *111*, 12512-12516.
- (39) Groothaert, M. H.; Pierloot, K.; Delabie A.; Schoonheydt, R. A. *Phys. Chem. Chem. Phys.* **2003**, *5*, 2135-2144.
- (40) Pietrzyk, P.; Sojka, Z. *J. Phys. Chem. A* **2005**, *109*, 10571-10581.
- (41) Pietrzyk, P.; Podolska, K.; Sojka, Z. *J. Phys. Chem. C* **2011**, *115*, 13008-13015.
- (42) Gaussian 09, Revision A.02, Frisch, M. J.; Trucks, G. W.; Schlegel, et al. Gaussian, Inc., Wallingford CT, 2009.
- (43) Becke, A. D. *J. Chem. Phys.* **1993**, *98*, 5648-5652.
- (44) (a) McLean, A. D.; Chandler, G. S. *J. Chem. Phys.* **1980**, *72*, 5639-48; (b) Wachters, A. J. *H. J. Chem. Phys.* **1970**, *52*, 1033-1036.
- (45) Li, X.; Frisch, M. J. *J. Chem. Theory Comput.* **2006**, *2*, 835-839.
- (46) Mitoraj, M.; Michalak, A. *J. Mol. Model.* **2007**, *13*, 347-355.
- (47) Michalak, A.; Mitoraj, M.; Ziegler, T. *J. Phys. Chem. A* **2008**, *112*, 1933-1939.



- 
- (48) te Velde, G.; Bickelhaupt, F. M.; Baerends, E. J.; Fonseca Guerra, C.; van Gisbergen, S. J. A.; Snijders, J. G.; Ziegler, T. *J. Comput. Chem.* **2001**, *22*, 931-967.
- (49) ADF2009.01, SCM, Theoretical Chemistry, Vrije Universiteit, Amsterdam, The Netherlands (<http://www.scm.com>).
- (50) Neese, F. ORCA – An *ab initio*, Density Functional and Semiempirical Program Package, Version 2.6-00, (Lehrstuhl für Theoretische Chemie, Bonn, 2007).
- (51) Neese, F. *J. Chem. Phys.* **2001**, *115*, 11080-11096.
- (52) Schreckenbach, G.; Ziegler, T. *J. Phys. Chem. A* **1997**, *101*, 3388-3399.
- (53) Neese, F. *J. Chem. Phys.* **2003**, *118*, 3939-3948.
- (54) Neese, F. *Inorg. Chim. Acta* **2002**, *337C*, 181-192.
- (55) Kieber-Emmons, M. T.; Riordan, C. G. *Acc. Chem. Res.* **2007**, *40*, 618-625.
- (56) Góra-Marek, K.; Glanowska, A.; Datka, J. *Micropor. Mesopor. Mater.* **2012**, *158*, 162-169.
- (57) Bonnevoit, L.; Olivier, D.; Che, M. *J. Mol. Catal.* **1983**, *21*, 415-430.
- (58) Freude, D.; Klinowski, J.; Hamdan, H. *Chem. Phys. Lett.* **1988**, *149*, 355-362.
- (59) Hunger, M.; Horvath, T. *J. Am. Chem. Soc.* **1996**, *118*, 12302-12308.
- (60) Mabbs, F. E.; Collison, D. *Electron paramagnetic resonance of d transition metal compounds*, Elsevier, The Netherlands, 1992, p. 427.

---

(61) Goodman, B. A.; Raynor, J. B. *Electron spin resonance of transition metal complexes* in Emeléus, H. J.; Sharpe, A. G. (Ed.) *Adv. Inorg. Chem. Radiochem.* **1970**, *13*, 135–362.

(62) Schreckenbach, G.; Ziegler, T. *J. Phys. Chem.* **1995**, *99*, 606-611.

(63) Lupinetti, A. J.; Fau, S.; Frenking, G.; Strauss, S. H. *J. Phys. Chem. A* **1997**, *101*, 9551-9559.